Supplementary Information to "Measuring Quantum Geometric Tensor of Non-Abelian System in Superconducting Circuits"

Wen Zheng,[1,*] Jianwen Xu,[1,*] Zhuang Ma,[1] Yong Li,[1] Yuqian Dong,[1] Yu Zhang,[1] Xiaohan Wang,[1] Guozhu Sun,[2] Peiheng Wu,[2] Jie Zhao,[1] Shaoxiong Li,[1] Dong Lan,[1,†] Xinsheng Tan,[1,‡] and Yang Yu[1,§]

[1] *National Laboratory of Solid State Microstructures, School of Physics, Nanjing University, Nanjing 210093, China*

[2] *School of Electronic Science and Engineering, Nanjing University, Nanjing 210093, China*

CONTENTS

I. SAMPLE INFORMATION AND EXPERIMENTAL SETUP

Sample and wiring diagram.— The four-qubit superconducting processor used in our experiment, whose parameters are summarized in Table S1 and Table S2, is composed of four tunable and grounded transmon qubits (It is also known as Xmon qubits) [1, 2]. We designed nearest-neighbor (N. N.) coupling strength $2J_{kl} \simeq 40$ MHz and next-nearest-neighbor (N. N. N) interactions $\sim 2J_{kl}/5$. As shown in Fig. S1(b), all transmons include a 'cross' shape capacitance to suppress charge noise, which is connected to ground through two Josephson junctions. Therefore, the transmons manipulation can be adjusted by inductively coupled Z lines and capacitively coupled XY lines. The counterparts of the above items in the circuit diagram are shown in Fig. S1(a). In addition, a readout resonator, one port coupled to a transmission line, is introduced to dispersively interact with each transmon. The effective N. N. and N. N. N. coupling strength can be further tuned by designing a suitable energy level structure according to the function of flux bias for the transition frequencies between $|0\rangle$ and $|1\rangle$ of four qubits, as shown in Fig. S2. The sample is fabricated with the following procedures:

(i) Clean a c-plane sapphire wafer by using the UV Ozone cleaner.

* These authors contributed equally to this work.
† land@nju.edu.cn
‡ tanxs@nju.edu.cn
§ yuyang@nju.edu.cn

TABLE S1. Device parameters.

	TQ_1	TQ_2	TQ_3	TQ_4
$\omega_q/2\pi$ [a] (GHz)	4.65217 (3.92158)	3.72558 (3.72558)	4.56861 (3.47061)	3.69262 (3.62361)
$\omega_r/2\pi$ [b] (GHz)	7.03038	7.08266	7.12667	7.16385
$\kappa_r/2\pi$ [c] (kHz)	39	161	32	65
$\chi_r/2\pi$ [d] (kHz)	41	26	32	27
$J_{r,q}/2\pi$ [e] (MHz)	44.7	48.2	41.2	51.2
T_1 [f] (µs)	45.6	39.0	41.8	31.5
T_2^* [h] (µs)	1.58	1.10	0.97	1.02

[a] Transition frequency $|0\rangle \rightarrow |1\rangle$ at the sweet spot (working point).
[b] Readout resonator frequency.
[c] Readout resonator intrinsic loss rate.
[d] Effective dispersive shift for the $|0\rangle \rightarrow |1\rangle$ transition due to the interaction with the readout cavity mode.
[e] Capacitively coupling strength between transmon and readout resonator derived by the dispersive shift [1].
[f] Energy decay time (T_1) measured at the working point.
[h] Ramsey decay time (T_2^*) measured at the working point.

(ii) Deposit about 100 nm aluminum on the sapphire by electron beam evaporation.

(iii) Define the large features of the processor by photolithography and wet etch, which include a transmission line, readout resonators, flux lines, and pads of the transmons.

(iv) Use the e-beam lithography technique, which realizes the strongly asymmetric controlled undercut structures by using a bilayer resist (MMA-MAA EL11 and PMMA A4) and protective coating(AR-PC 5090.02), to define the Josephson junctions.

(v) Apply double-angle evaporation technique [3] to define the Al/AlO(x)/Al junctions.

(vi) Introduce the airbridge to suppress the flux and drive crosstalk [4], with the process as follows: pattern and reflow the photoresist, deposit at least 400 nm aluminum, define the bridge using photolithography, and wet etch the excess aluminum.

(vii) And finally, package the processor after lift-off.

The diagram of the measurement setup is shown in Fig. S1(c). In our experiment, we use the Z lines to modulate the frequencies of transmons, the Probe and Output lines to readout quantum states, and the XY drive lines to initialize and manipulate quantum states, respectively. All input signals (including the Probe signal) are generated in the room-temperature electronic part (translucent red) and then sent to the processor after appropriate attenuation and isolation in the cryogenic part (translucent turquoise) as shown in the diagram, respectively. The Output signal is amplified by a high-electron-mobility-transistor (HEMT) at 4 Kelvin stage in the dilution refrigerator and two low noise amplifiers at room temperature, and finally, the IQ mixer is used to demodulate it into an IF signal, which is collected by ADCs.

Circuit quantization.— As shown in Fig. S1(a), in our system based on circuit analysis [1, 5], the Lagrangian can be written as

$$\mathcal{L} = \mathcal{T} - \mathcal{U} \tag{S1}$$

with

$$\mathcal{T} = \sum_k \frac{1}{2} C_k \dot{\Phi}_k^2 + \sum_{kl} \frac{1}{2} C_{kl} (\dot{\Phi}_k - \dot{\Phi}_l)^2 = \frac{1}{2} \dot{\Phi}^T C \dot{\Phi}, \tag{S2}$$

$$\mathcal{U} = -\sum_k E_{J_k} \cos(\Phi_k), \tag{S3}$$

where qubits denote as $k \in \{1, 2, 3, 4\}$, $kl \in \{12, 23, 34, 41\}$, the flux is $\Phi = [\Phi_1, \Phi_2, \Phi_3, \Phi_4]$, and the four-by-four capacitance matrix C is

$$C = \begin{bmatrix} C_1 + C_{12} + C_{13} + C_{41} & -C_{12} & -C_{13} & -C_{41} \\ -C_{12} & C_{12} + C_2 + C_{34} + C_{24} & -C_{34} & -C_{24} \\ -C_{13} & -C_{34} & C_{13} + C_{34} + C_3 + C_{34} & -C_{34} \\ -C_{41} & -C_{24} & -C_{34} & C_{41} + C_{24} + C_{34} + C_4 \end{bmatrix}. \tag{S4}$$

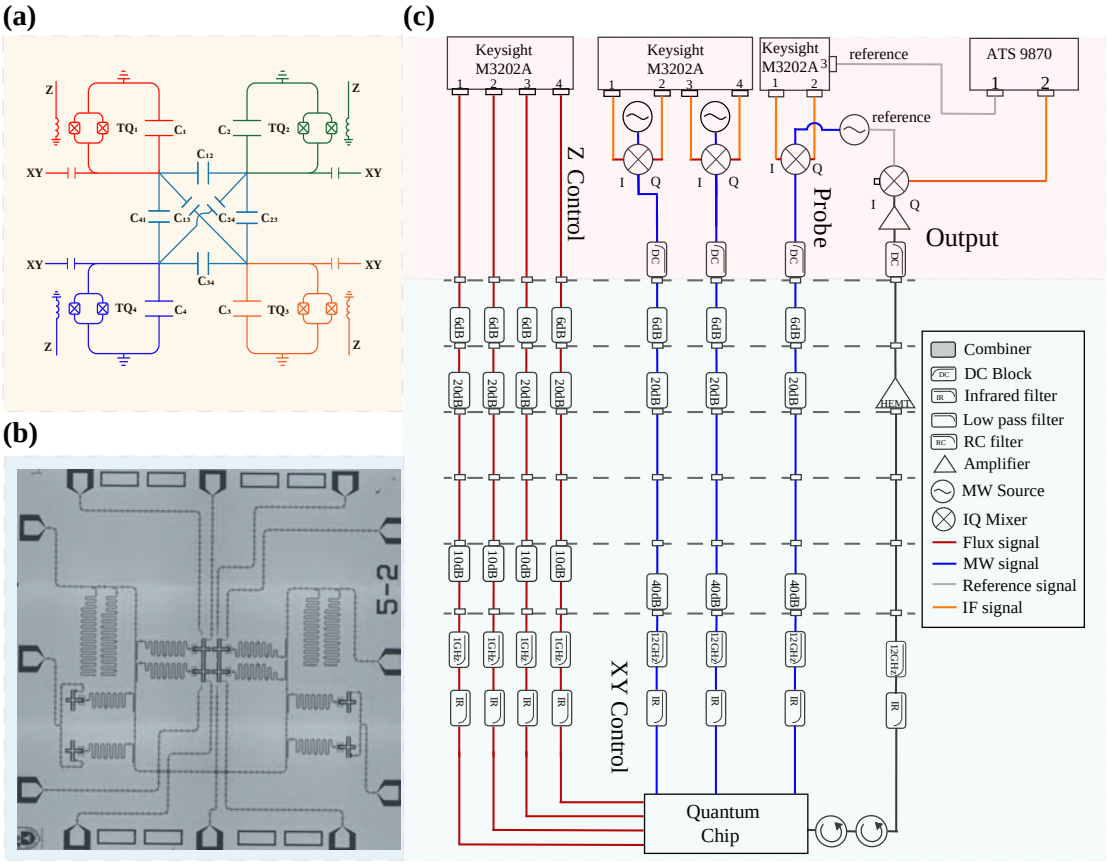

FIG. S1. **Sample and measuremental setup.** **(a)** A circuit diagram of the four-qubit processor. They are labeled as TQ_1, TQ_2, TQ_3, TQ_4, respectively. **(b)** Full image of the quantum processor which contains four transmons. **(c)** Experimental diagram for quantum control and readout. The microwave waveforms for XY control and probe are produced by up-conversion technique. The details include generating a local carrier from microwave source, manipulating intermediate frequency (IF) signals by using arbitrary waveform generator (AWG), and then synthesizing the controllable waveforms by using IQ mixer. For Z control, the static flux bias signals and longitudinal parametric pulses are directly generated by Keysight-M3202A. In order to achieve cryogenic quantum control and probe, all signals are attenuated and filtered before sent into the quantum chip through corresponding lines. For readout, the output signal passes through two circulators and then is filtered after the probe signal with quantum state information comes out of the chip. Next, it is amplified by a high-electron-mobility-transistor (HEMT) at low temperature, and is amplified again by low noise amplifiers after coming out of the fridge to increase signal noise ratio (SNR). Before digital processing by an ADC channel (ATS-9870), the readout signal is down-converted to IF signals and the another channel of ATS-9870 board received an IF signal from Keysight-M3202A to provide a reference phase.

By introducing the charge $Q = C\dot{\Phi} = [\partial\mathcal{L}/\partial\dot{\Phi}_1, \partial\mathcal{L}/\partial\dot{\Phi}_2, \partial\mathcal{L}/\partial\dot{\Phi}_3, \partial\mathcal{L}/\partial\dot{\Phi}_4]$, which is a conjugate variable to the flux Φ, the classical Hamiltonian $\mathcal{H}_0$ can be expressed as

$$\mathcal{H}_0 = Q\dot{\Phi} - \mathcal{L} = \frac{1}{2}Q^T C^{-1} Q + \mathcal{U}, \tag{S5}$$

where C^{-1} is the inverse capacitance matrix

$$C^{-1} = \frac{1}{|C|}\begin{bmatrix} A_{11} & A_{12} & A_{13} & A_{41} \\ A_{12} & A_{22} & A_{34} & A_{24} \\ A_{13} & A_{34} & A_{33} & A_{34} \\ A_{41} & A_{24} & A_{34} & A_{44} \end{bmatrix}, \tag{S6}$$

with the determinant term

$$\begin{aligned} |C| \approx\ & C_1C_2C_3C_4 + C_1C_2C_3C_{41} + C_1C_2C_4C_{13} + C_1C_2C_3C_{24} + C_1C_2C_4C_{34} + C_1C_2C_3C_{34} + C_1C_2C_4C_{34} \\ & + C_1C_3C_4C_{12} + C_1C_3C_4C_{34} + C_1C_3C_4C_{24} + C_2C_3C_4C_{12} + C_2C_3C_4C_{13} + C_2C_3C_4C_{41}, \end{aligned}$$

the diagonal terms

$$A_{11} \approx C_2C_3C_4 + C_2C_3C_{41} + C_2C_4C_{13} + C_3C_4C_{12} + C_2C_3C_{24} + C_2C_4C_{34} + C_3C_4C_{34} + C_3C_4C_{24} + C_2C_3C_{34} + C_2C_4C_{34},$$
$$A_{22} \approx C_1C_3C_4 + C_1C_3C_{41} + C_1C_4C_{13} + C_3C_4C_{12} + C_3C_4C_{13} + C_3C_4C_{41} + C_1C_3C_{24} + C_1C_4C_{34} + C_1C_3C_{34} + C_1C_4C_{34},$$
$$A_{33} \approx C_1C_2C_4 + C_1C_2C_{41} + C_1C_4C_{12} + C_2C_4C_{12} + C_2C_4C_{13} + C_2C_4C_{41} + C_1C_2C_{24} + C_1C_4C_{34} + C_1C_4C_{24} + C_1C_2C_{34},$$
$$A_{44} \approx C_1C_2C_3 + C_1C_2C_{13} + C_1C_3C_{12} + C_2C_3C_{12} + C_2C_3C_{13} + C_2C_3C_{41} + C_1C_2C_{34} + C_1C_3C_{34} + C_1C_3C_{24} + C_1C_2C_{34},$$

and the non-diagonal terms

$$A_{12} \approx C_3C_4C_{12} + C_3C_{12}C_{41} + C_4C_{12}C_{13} + C_3C_{12}C_{24} + C_4C_{12}C_{34} + C_4C_{13}C_{34} + C_3C_{41}C_{24} + C_3C_{12}C_{34} + C_4C_{12}C_{34},$$
$$A_{13} \approx C_2C_4C_{13} + C_2C_{13}C_{41} + C_4C_{12}C_{13} + C_2C_{13}C_{24} + C_4C_{12}C_{34} + C_4C_{13}C_{34} + C_4C_{13}C_{24} + C_2C_{13}C_{34} + C_2C_{41}C_{34},$$
$$A_{41} \approx C_2C_3C_{41} + C_2C_{13}C_{41} + C_3C_{12}C_{41} + C_2C_{41}C_{34} + C_3C_{12}C_{24} + C_3C_{41}C_{34} + C_3C_{41}C_{24} + C_2C_{13}C_{34} + C_2C_{41}C_{34},$$
$$A_{34} \approx C_1C_4C_{34} + C_4C_{12}C_{13} + C_1C_{41}C_{34} + C_4C_{12}C_{34} + C_4C_{13}C_{34} + C_4C_{41}C_{34} + C_1C_{34}C_{24} + C_1C_{34}C_{34} + C_1C_{24}C_{34},$$
$$A_{24} \approx C_1C_3C_{24} + C_3C_{12}C_{41} + C_1C_{13}C_{24} + C_3C_{12}C_{24} + C_3C_{13}C_{24} + C_3C_{41}C_{24} + C_1C_{34}C_{24} + C_1C_{34}C_{34} + C_1C_{24}C_{34},$$
$$A_{34} \approx C_2C_{13}C_{41} + C_1C_2C_{34} + C_1C_{12}C_{34} + C_1C_{34}C_{24} + C_2C_{12}C_{34} + C_2C_{13}C_{34} + C_2C_{41}C_{34} + C_1C_{34}C_{34} + C_1C_{24}C_{34}.$$

After canonical quantization, the Hamiltonian $\mathcal{H}_0$ reads

$$\mathcal{H}_0 = \sum_{k=1}^{4}(4E_{C_k}n_k^2 - E_{J_k}\cos(\phi_k)) + \sum_{kl} 4E_{kl}n_kn_l, \tag{S7}$$

where $n_k = Q_k/2e$, $\phi_k = 2\pi\Phi_k/\Phi_0$, $E_{C_k} = A_{kk}e^2/(2|C|)$, and E_{J_k}, $E_{kl} = A_{kl}e^2/|C|$ are Cooper pair number operators, reduced flux operators, charging energies, Josephson energies, and coupling energies, respectively, while e is the electric charge of a single electron.

We rewrite the operators $n_k = \frac{i}{\sqrt{2}}(E_{J_k}/8E_{C_k})^{1/4}(a_k^\dagger - a_k)$ and $\phi_k = \frac{1}{2}(8E_{C_k}/E_{J_k})^{1/4}(a_k^\dagger + a_k)$ to define annihilation and creation operators $a_k^\dagger$, a_k. Hence, expanding the cosine in Eq. S7 around $\phi_k = 0$ up to fourth order, and treating the resulting quartic term in leading order perturbation theory, the Eq. (S7) can be rewritten as

$$\mathcal{H}_0 \simeq \sum_{k=1}^{4}(\hbar\omega_k a_k^\dagger a_k - \frac{E_{C_k}}{2}a_k^\dagger a_k^\dagger a_k a_k) + \sum_{kl} J_{kl}(a_k^\dagger a_l + a_k a_l^\dagger), \tag{S8}$$

where the frequency of the k-th qubit is

$$\omega_k \simeq (\sqrt{8E_{C_k}E_{J_k}} - E_{C_k})/\hbar \tag{S9}$$

and the qubit-qubit coupling strength is $J_{kl} = \frac{E_{kl}}{\sqrt{2}}\left(\frac{E_{J_k}E_{J_l}}{E_{C_k}E_{C_l}}\right)^{\frac{1}{4}}$.

Based on circuit quantization, one can obtain the designed parameters of the four-qubit processor in fabrication. For instance, in our experiment, the 'cross' shape capacitance in parallel with the Josephson junctions is about 65 fF, the capacitance between the N. N. qubits is approximately 0.619 fF, and the capacitance between the N. N. N qubits is about 0.138 fF. Correspondingly, the key parameters E_{C_l} and J_{kl} we designed and measured are listed in Table S2.

TABLE S2. Paremeters in fabrication

	$E_{C_1}/2\pi$	$E_{C_2}/2\pi$	$E_{C_3}/2\pi$	$E_{C_4}/2\pi$	$g_{12}/2\pi$	$g_{13}/2\pi$	$g_{41}/2\pi$	$g_{23}/2\pi$	$g_{24}/2\pi$	$g_{34}/2\pi$
designed (MHz)	292.1	292.1	292.1	292.1	20.45	5.44	20.37	20.53	4.44	20.45
measured (MHz)	283	–	–	–	18.8	4.0	17.5	18.0	3.5	16.7

II. REALIZATION OF NON-ABELIAN SYSTEM IN SUPERCONDUCTING CIRCUIT

Longitudinal parametric modulation.— In order to construct a non-Abelian system in our four-qubit system, we introduce a sinusoidal pulse $\Phi_m = \bar{\Phi}_m + \delta\Phi_{kl}\cos(\Delta_{kl}t + \varphi_{kl}) + \delta\Phi_{k'l'}\cos(\Delta_{k'l'}t + \varphi_{k'l'})$ into each modulating qubit TQ_m ($m = 1, 3$ denote the tunable qubits.), where the parking point of the m-th transmon is biased by $\bar{\Phi}_m$, and the amplitudes $\delta\Phi_{kl,k'l'}$, the angular frequencies $\Delta_{kl,k'l'}$ and the phases $\varphi_{kl,k'l'}$ can be parametric modulation conveniently

TABLE S3. Flux crosstalk

	TQ_1	TQ_2	TQ_3	TQ_4
TQ_1	1.	-0.006	-0.009	-0.019
TQ_2	0.002	1.	-0.02	-0.009
TQ_3	0.003	0.019	1.	-0.004
TQ_4	0.017	-0.001	-0.03	1.

by AWG. Since the qubit frequency ω_m nonlinearly depends on the flux modulation according to Eq. (S9) and can be described by a Taylor series with non-trivial higher-order terms [6], there are terms that can be approximately expanded as

$$\begin{aligned}
\omega_m(t) \approx & \omega_m(\bar{\Phi}_m) + \frac{\partial \omega_m(\Phi_m)}{\partial \Phi_m}\Big|_{\bar{\Phi}_m} \left[\omega_{kl}^T \cos(\Delta_{kl} t + \varphi_{kl}) + \omega_{k'l'}^T \cos(\Delta_{k'l'} t + \varphi_{k'l'})\right] \\
& + \frac{1}{2}\frac{\partial^2 \omega_m(\Phi_m)}{\partial \Phi_m^2}\Big|_{\bar{\Phi}_m} \left[\omega_{kl}^T \cos(\Delta_{kl} t + \varphi_{kl}) + \omega_{k'l'}^T \cos(\Delta_{k'l'} t + \varphi_{k'l'})\right]^2, \\
= & \omega_m(\bar{\Phi}_m) + \frac{1}{4}\frac{\partial^2 \omega_m(\Phi_m)}{\partial \Phi_m^2}\Big|_{\bar{\Phi}_m} \left[(\omega_{k'l'}^T)^2 + (\omega_{kl}^T)^2\right] \\
& + \frac{\partial \omega_m(\Phi_m)}{\partial \Phi_m}\Big|_{\bar{\Phi}_m} \left[\omega_{kl}^T \cos(\Delta_{kl} t + \varphi_{kl}) + \omega_{k'l'}^T \cos(\Delta_{k'l'} t + \varphi_{k'l'})\right] \\
& + \frac{1}{4}\frac{\partial^2 \omega_m(\Phi_m)}{\partial \Phi_m^2}\Big|_{\bar{\Phi}_m} \left[(\omega_{kl}^T)^2 \cos(2\Delta_{kl} t + 2\varphi_{kl}) + (\omega_{k'l'}^T)^2 \cos(2\Delta_{k'l'} t + 2\varphi_{k'l'})\right] \\
& + \frac{1}{2}\frac{\partial^2 \omega_m(\Phi_m)}{\partial \Phi_m^2}\Big|_{\bar{\Phi}_m} \omega_{kl}^T \omega_{k'l'}^T \left[\cos((\Delta_{kl} + \Delta_{k'l'})t + \varphi_{kl} + \varphi_{k'l'}) + \cos((\Delta_{kl} - \Delta_{k'l'})t + \varphi_{kl} - \varphi_{k'l'})\right],
\end{aligned} \tag{S10}$$

under the parking spot $\omega_m(\bar{\Phi}_m)$ that is biased by flux $\bar{\Phi}_m$ and parked away from the sweet spot. Here, the amplitude ω_{kl}^T are the 1st-order approximation for the response of the flux modulation amplitude $\delta\Phi_{kl}$ in the spectrum of qubit TQ_m, frequency Δ_{kl} and phase φ_{kl} are the sinusoidal pulse parameters, all of them are required for calibration in experiment to exquisitely control the coupling term between qubits TQ_m and its N. N. qubits. After introducing $\hbar = 1$, the Eq. (S8) becomes

$$\begin{aligned}
H_L = & \omega_1(t) a_1^\dagger a_1 + \omega_2 a_2^\dagger a_2 + \omega_3(t) a_3^\dagger a_3 + \omega_4 a_4^\dagger a_4 \\
& - \frac{E_{C_1}}{2} a_1^\dagger a_1^\dagger a_1 a_1 - \frac{E_{C_2}}{2} a_2^\dagger a_2^\dagger a_2 a_2 - \frac{E_{C_3}}{2} a_3^\dagger a_3^\dagger a_3 a_3 - \frac{E_{C_4}}{2} a_4^\dagger a_4^\dagger a_4 a_4 \\
& + J_{12}(a_1^\dagger + a_1)(a_2^\dagger + a_2) + J_{41}(a_1^\dagger + a_1)(a_4^\dagger + a_4) \\
& + J_{34}(a_3^\dagger + a_3)(a_2^\dagger + a_2) + J_{34}(a_3^\dagger + a_3)(a_4^\dagger + a_4).
\end{aligned} \tag{S11}$$

In order to transform H_L to interacting picture, a unitary operator $U = e^{iF_1(t)a_1^\dagger a_1} \otimes e^{i\omega_2 a_2^\dagger a_2} \otimes e^{iF_3(t)a_3^\dagger a_3} \otimes e^{i\omega_4 a_4^\dagger a_4}$ is introduced with defining functions $F_1(t) = \int \omega_1(t)dt$ and $F_3(t) = \int \omega_3(t)dt$. Then, the function $F_m(t)$ can be approximated by

$$\begin{aligned}
F_m(t) \approx & \overline{\omega}_m(t) \cdot t + \frac{\partial \omega_m(\Phi_m)}{\partial \Phi_m}\Big|_{\bar{\Phi}_m} \left[\frac{\omega_{kl}^T}{\Delta_{kl}} \sin(\Delta_{kl} t + \varphi_{kl}) + \frac{\omega_{k'l'}^T}{\Delta_{k'l'}} \sin(\Delta_{k'l'} t + \varphi_{k'l'})\right] \\
& + \frac{1}{4}\frac{\partial^2 \omega_m(\Phi_m)}{\partial \Phi_m^2}\Big|_{\bar{\Phi}_m} \left[\frac{(\omega_{kl}^T)^2}{2\Delta_{kl}} \sin(2\Delta_{kl} t + 2\varphi_{kl}) + \frac{(\omega_{k'l'}^T)^2}{2\Delta_{k'l'}} \sin(2\Delta_{k'l'} t + 2\varphi_{k'l'})\right] \\
& + \frac{1}{2}\frac{\partial^2 \omega_m(\Phi_m)}{\partial \Phi_m^2}\Big|_{\bar{\Phi}_m} \left[\frac{\omega_{kl}^T \omega_{k'l'}^T}{\Delta_{kl} + \Delta_{k'l'}} \sin\left[(\Delta_{kl} + \Delta_{k'l'})t + \varphi_{kl} + \varphi_{k'l'}\right] + \frac{\omega_{kl}^T \omega_{k'l'}^T}{\Delta_{kl} - \Delta_{k'l'}} \sin\left[(\Delta_{kl} - \Delta_{k'l'})t + \varphi_{kl} - \varphi_{k'l'}\right]\right].
\end{aligned} \tag{S12}$$

Here, $\overline{\omega}_m(t) = \omega_m(\bar{\Phi}_m) + \frac{1}{4}\frac{\partial^2 \omega_m(\Phi_m)}{\partial \Phi_m^2}\Big|_{\bar{\Phi}_m} \left[(\omega_{k'l'}^T)^2 + (\omega_{kl}^T)^2\right]$ is the mean frequency of TQ_m during the longitudinal parametric modulation. In addition, the parameters $\varphi_{kl,k'l'}$, $\Delta_{kl,k'l'}$, and $\omega_{kl,k'l'}^T$ will slowly vary with time t under the weak parametric modulation fields driving, to meet the condition to measure the quantum geometric tensor based on coherent Rabi oscillations (Details see Section V), ensuring that the modulated frequency ω of the

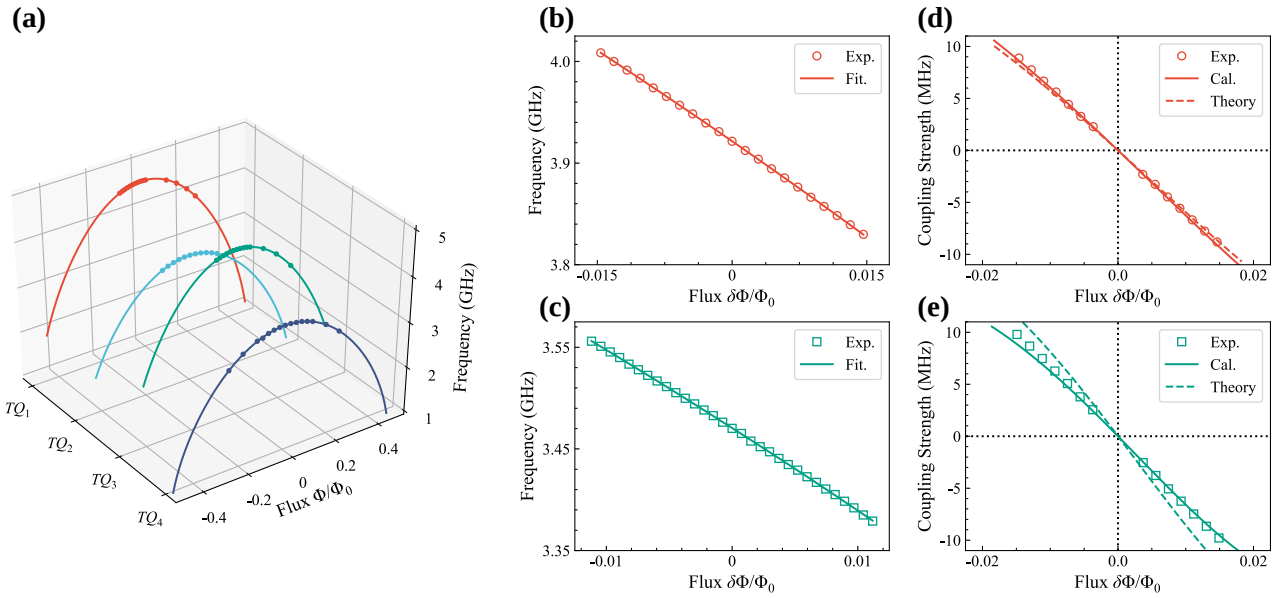

FIG. S2. **Calibrations for the measurement of the quantum geometric tensor. (a)** The spectrums of the superconducting processor. In experiment, the parking points of the fluxing qubits (TQ_1 and TQ_3) are $\Phi_1 = 0.248\Phi_0$ and $\Phi_3 = 0.297\Phi_0$, while the static qubits (TQ_2 and TQ_4) are biased at $\Phi_2 = 0$ and $\Phi_4 = 0.088\Phi_0$. **(b)** and **(c)** are the calibrations of the corresponding amplitudes $\delta\Phi$ of the longitudinal parametric modulations. **(b)** and **(c)** are the effective coupling strength Ω_1 and Ω_2 under the different longitudinal parametric modulation amplitudes $\delta\Phi$.

weak parametric modulation fields in Eq. (S29) meets $\omega \ll \Delta_{kl,k'l'}(t)$. Therefore, using Jacobi-Anger expansion $e^{iz\sin\varphi'_{kl}} = \sum_{-\infty}^{\infty}\mathcal{J}_n(z)e^{in\varphi'_{kl}}$, and neglecting the terms which are fast oscillation or about equal to 1 in the expansions [6, 7], the effective Hamiltonian under rotating wave approximation (RWA) can be written as

$$\begin{aligned} H_s \simeq\ & (\delta_{12}-\delta_{41})|0001\rangle\langle 0001| + (\delta_{23}-\delta_{12})|0010\rangle\langle 0010| \\ & + (\delta_{34}-\delta_{23})|0100\rangle\langle 0100| + (\delta_{41}-\delta_{23})|1000\rangle\langle 1000| \\ & + J_{12}\mathcal{J}_1(\frac{\omega_{12}^T}{\Delta_{12}})\mathcal{J}_0(\frac{\omega_{41}^T}{\Delta_{41}})e^{-i\varphi'_{12}}|0010\rangle\langle 0001| \\ & + J_{41}\mathcal{J}_0(\frac{\omega_{12}^T}{\Delta_{12}})\mathcal{J}_1(\frac{\omega_{41}^T}{\Delta_{41}})e^{-i\varphi'_{41}}|1000\rangle\langle 0001| \\ & + J_{23}\mathcal{J}_1(\frac{\omega_{23}^T}{\Delta_{23}})\mathcal{J}_0(\frac{\omega_{34}^T}{\Delta_{34}})e^{-i\varphi'_{23}}|0010\rangle\langle 0100| \\ & + J_{34}\mathcal{J}_0(\frac{\omega_{23}^T}{\Delta_{23}})\mathcal{J}_1(\frac{\omega_{34}^T}{\Delta_{34}})e^{-i\varphi'_{34}}|1000\rangle\langle 0100| \\ & + h.c. \end{aligned} \tag{S13}$$

where $\mathcal{J}_n$ is the first kind n-th order Bessel function, and the corresponding parameters are defined as

$$\begin{aligned} &\delta_{12} = \overline{\omega}_1 - \omega_2 - \Delta_{12}, \quad \varphi'_{12} = \varphi_{12} - (\frac{\omega_{12}^T}{\Delta_{12}}\sin\varphi_{12} + \frac{\omega_{41}^T}{\Delta_{41}}\sin\varphi_{41}), \\ &\delta_{23} = \overline{\omega}_3 - \omega_2 - \Delta_{23}, \quad \varphi'_{23} = \varphi_{23} - (\frac{\omega_{23}^T}{\Delta_{23}}\sin\varphi_{23} + \frac{\omega_{34}^T}{\Delta_{34}}\sin\varphi_{34}), \\ &\delta_{34} = \overline{\omega}_3 - \omega_4 - \Delta_{34}, \quad \varphi'_{34} = \varphi_{34} - (\frac{\omega_{23}^T}{\Delta_{23}}\sin\varphi_{23} + \frac{\omega_{34}^T}{\Delta_{34}}\sin\varphi_{34}), \\ &\delta_{41} = \overline{\omega}_1 - \omega_4 - \Delta_{41}, \quad \varphi'_{41} = \varphi_{41} - (\frac{\omega_{12}^T}{\Delta_{12}}\sin\varphi_{12} + \frac{\omega_{41}^T}{\Delta_{41}}\sin\varphi_{41}). \end{aligned} \tag{S14}$$

Realization of Non-Abelian system in Superconducting circuit.— According to Eq. (S7), the spectrum of a transmon, as shown in Fig. S2(a), can be calibrated by adjusting the flux Φ through the Z control line. The crosstalk of flux has

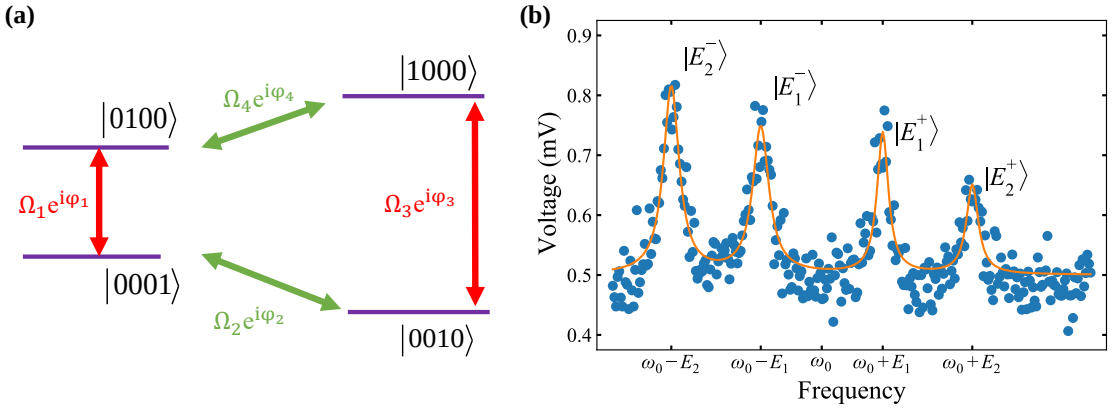

FIG. S3. **(a)** Illustration of the diamond shape Hamiltonian in our superconducting circuit. The coupling strength between each states are labeled as Ω_1, Ω_2 , Ω_3 , and Ω_4 respectively. **(b)** Experimental spectrum of the Eigenstates $E^{\pm}_{1,2}$, while the corresponding Hamiltonian is shown in (a). The frequency in the horizontal axis is replaced by the eigenvalues of Hamiltonian, with $E_1 = \sqrt{(\Omega_1^2+\Omega_2^2+\Omega_3^2+\Omega_4^2) - \sqrt{(\Omega_1^2+\Omega_2^2+\Omega_3^2+\Omega_4^2)^2 - 4[\Omega_1^2\Omega_3^2 - 2\Omega_1\Omega_2\Omega_3\Omega_4\cos(\varphi_1+\varphi_2+\varphi_3-\varphi_4)+\Omega_2^2\Omega_4^2]}/2}$, $E_2 = \sqrt{(\Omega_1^2+\Omega_2^2+\Omega_3^2+\Omega_4^2) + \sqrt{(\Omega_1^2+\Omega_2^2+\Omega_3^2+\Omega_4^2)^2 - 4[\Omega_1^2\Omega_3^2 - 2\Omega_1\Omega_2\Omega_3\Omega_4\cos(\varphi_1+\varphi_2+\varphi_3-\varphi_4)+\Omega_2^2\Omega_4^2]}/2}$, here Ω_i is set as $\Omega_1/2\pi = \Omega_2/2\pi = \Omega_3/2\pi = \Omega_4/2\pi$=2.5MHz, while $\varphi_1 = \varphi_2 = \varphi_4 = 0$, and $\varphi_3 = 0.3\pi$.

been calibrated as shown in Table S3, so that we can independently and accurately manipulate the energy diagram of each transmon. Therefore, as shown in Fig. 2(a) in main text, the energy diagram used in our experiment can be constructed by parking the transition frequencies between $|0\rangle$ and $|1\rangle$ at $TQ_1 = 3.92158$ GHz ($\Phi_1 = 0.248\Phi_0$, where Φ_0 is one flux quantum), $TQ_2 = 3.72558$ GHz ($\Phi_2 = 0$), $TQ_3 = 3.47061$ GHz ($\Phi_3 = 0.297\Phi_0$), and $TQ_4 = 3.62361$ GHz ($\Phi_4 = 0.088\Phi_0$), respectively. Here, to mitigate the spurious coupling tones, the qubits are parked away from each other by adjusting the detuning between the N. N. qubits, which is several orders of times larger than the N. N. N. coupling interactions.

Notice that, at these working points, although the phase decoherence times $T_2^\star$ are short, as shown in Table S1, because we concerned about the Rabi oscillation frequency Ω rather than the occupation of states, this ensures that more accurate results can be obtained even if the coherence time is relatively short. In addition, the Hilbert space composed of a set of special quantum states (including $|0001\rangle$, $|0010\rangle$, $|0100\rangle$, and $|1000\rangle$) is an intrinsic decoherence-free space, which is insensitive to longitudinal noise such as flux noise [8]. That means, for the modulating qubits (TQ_1 and TQ_3), we can choose the more conveniently controllable points (Φ_1 and Φ_3) to facilitate the longitudinal parametric modulations.

Moreover, based on the above analysis, the parameters in Eq. (S13) can be accurately calibrated with routine methods. For instance, as shown in Fig. S2(b) and (c), the sinusoidal waveforms of the modulating qubits can be acquired by spectroscopy measurement. The effective coupling strength as a function of flux under parametric modulation, as shown in Fig. S2(d) and (e), can be extracted by the oscillation of population between qubits. The detuning δ_{kl} and the phase $\varphi_{kl}^{'}$ can be calibrated by Ramsey interference measurement. It is noteworthy that, as shown in Fig. S2(d) and (e), due to the difference in the amplitude-frequency response in experimental circuits, the effective coupling strength corresponding to the waveform with different modulating frequencies in calibration (the points) will be different from the predicted value (the dashed lines) obtained according to Eq. (S12). Comparatively, the lines stand by the theoretical predictions with the correction considering the amplitude-frequency response. Therefore, this difference should be considered in the calibrations. And finally, as show in Fig. S3(a), a diamond Hamiltonian based on Eq. (S13) can be exquisitely manipulated with the flux parametric modulation pulses Φ_m. The modulated terms $\Omega_i e^{i\varphi_i}$ therein correspond to the coupling strength between two transmons in Eq. S13, e.g. $\Omega_1 e^{i\varphi_1} = J_{12}\mathcal{J}_1(\frac{\omega_{12}^T}{\Delta_{12}})\mathcal{J}_0(\frac{\omega_{41}^T}{\Delta_{41}})e^{i\varphi'_{12}}$. The eigenvalues of a diamond Hamiltonian can be calibrated by spectroscopy measurement in experiment as illustrated in Fig. S3(b).

To conclude, the non-Abelian system synthesized by transmons can be constructed by adjusting the corresponding parameters of the longitudinal parametric modulation. For instance, the widely used non-Abelian model $H(\lambda) = d_0(\lambda) + \sum_{k=1}^{5} d_k(\lambda)\Gamma_k$, which is the one of the most important toy model to understand the topological properties in physics, can be realized based on Eq. (S13) and Eq. (S14). Here, $d_0(\lambda)$ and $d_k(\lambda)$ are real functions of the parameter $\lambda = (\lambda_1, \lambda_2, \lambda_3, \lambda_4, \lambda_5)$, and the Dirac matrices Γ_k satisfy $\{\Gamma_k, \Gamma_{k'}\} = 2\delta_{kk'}$.

III. BERNEVIG–HUGHES–ZHANG MODEL

In this article, we choose the Bernevig–Hughes–Zhang (BHZ) model to demonstrate the validity of our approach. BHZ model effectively describes the spin Hall effect under the time-reversal symmetry in the system of two-dimensional time-reversal-invariant topological insulator HgTe/CdTe quantum wells [13–15], which describe the spin Hall effect under the time-reversal symmetry [16–20]. The Hamiltonian is written as

$$H_{BHZ} = \begin{bmatrix} B_z & 0 & B_x - iB_y & B_g \\ 0 & B_z & B_g & -B_x - iB_y \\ B_x + iB_y & B_g & -B_z & 0 \\ B_g & -B_x + iB_y & 0 & -B_z \end{bmatrix} \tag{S15}$$

where $B_x = H_{xy} \sin k_x, B_y = H_{xy} \sin k_y, B_z = M - 2H_z(2 - \cos k_x - \cos k_y)$. The momentum k_x, k_y are constrained to $[-\pi, \pi]$ and the material parameters which depend on the quantum well geometry are labeled as H_{xy}, M, and H_z. The Hamiltonian eigenvalues $E_\pm = \pm\sqrt{B_x^2 + B_y^2 + B_z^2 + B_g^2}$.

In the sphere coordinate, the Eq. (S15) can be parameterized as

$$H = \frac{H_{BHZ}}{|E_\pm|} = \begin{bmatrix} \cos\theta & 0 & e^{-i\varphi}\sin\theta\sin\gamma & \sin\theta\cos\gamma \\ 0 & \cos\theta & \sin\theta\cos\gamma & -e^{i\varphi}\sin\theta\sin\gamma \\ e^{i\varphi}\sin\theta\sin\gamma & \sin\theta\cos\gamma & -\cos\theta & 0 \\ \sin\theta\cos\gamma & -e^{-i\varphi}\sin\theta\sin\gamma & 0 & -\cos\theta \end{bmatrix} \tag{S16}$$

where $\theta = \arctan\frac{\Omega_1}{B_z}$, $\gamma = \arctan\frac{\Omega_2}{B_g}$, and $\varphi = \arctan\frac{B_y}{B_x}$, respectively, with $\theta \in [0, \pi]$, $\gamma \in [0, \pi]$, $\varphi \in [0, 2\pi]$, respectively. The energy parameters are $\Omega_1 = \sqrt{B_x^2 + B_y^2 + B_g^2}$ and $\Omega_2 = \sqrt{B_x^2 + B_y^2}$. The eigenstates can be written as

$$\begin{aligned} |\psi_1^-\rangle &= \begin{bmatrix} \sin\gamma\cos\frac{\theta}{2} \\ e^{i\varphi}\sin\frac{\theta}{2} \\ e^{i\varphi}\cos\frac{\theta}{2}\cos\gamma \\ 0 \end{bmatrix}, \qquad |\psi_2^-\rangle = \begin{bmatrix} e^{-i\varphi}\cos\frac{\theta}{2}\cos\gamma \\ 0 \\ -\sin\gamma\cos\frac{\theta}{2} \\ e^{-i\varphi}\sin\frac{\theta}{2} \end{bmatrix}, \\ |\psi_1^+\rangle &= \begin{bmatrix} \sin\frac{\theta}{2}\sin\gamma \\ -e^{i\varphi}\cos\frac{\theta}{2} \\ e^{i\varphi}\sin\frac{\theta}{2}\cos\gamma \\ 0 \end{bmatrix}, \qquad |\psi_2^+\rangle = \begin{bmatrix} -e^{-i\varphi}\sin\frac{\theta}{2}\cos\gamma \\ 0 \\ \sin\frac{\theta}{2}\sin\gamma \\ e^{-i\varphi}\cos\frac{\theta}{2} \end{bmatrix} \end{aligned} \tag{S17}$$

with the eigenvalues $E_\pm = \pm 1$.

Notice the manifold of the quantum state is sphere surface S3 in the Hilbert space, while the Hamiltonian is a non-Abelian one. We can derive its topological and geometric properties step by step. First is the gauge potential, the non-Abelian Berry connection is defined as

$$A_{nm}^{\mu}(\lambda) = i\langle\psi_n|\frac{\partial}{\partial\lambda_\mu}|\psi_m\rangle \tag{S18}$$

Then, the corresponding vector gauge fields read

$$\begin{aligned} A^\theta &= \begin{bmatrix} 0 & 0 \\ 0 & 0 \end{bmatrix}, \quad A^\gamma = \cos^2\frac{\theta}{2}\begin{bmatrix} 0 & -e^{-i\varphi} \\ e^{i\varphi} & 0 \end{bmatrix}, \\ A^\varphi &= i\frac{\theta}{2}\begin{bmatrix} \sin^2\frac{\theta}{2} + \cos^2\frac{\theta}{2}\cos^2\gamma & -\cos^2\frac{\theta}{2}\sin\gamma\cos\gamma e^{-i\varphi} \\ -\cos^2\frac{\theta}{2}\sin\gamma\cos\gamma e^{i\varphi} & -\sin^2\frac{\theta}{2}\sin^2\gamma - \cos^2\gamma \end{bmatrix} \end{aligned} \tag{S19}$$

with the relationships of commutation

$$\begin{aligned} [A^\theta, A^\gamma] &= \begin{bmatrix} 0 & 0 \\ 0 & 0 \end{bmatrix}, \quad [A^\theta, A^\varphi] = \begin{bmatrix} 0 & 0 \\ 0 & 0 \end{bmatrix}, \\ [A^\gamma, A^\varphi] &= i\cos^2\frac{\theta}{2}\begin{bmatrix} \cos^2\frac{\theta}{2}\sin\gamma\cos\gamma & \left(1 - 2\cos^2\frac{\theta}{2}\sin^2\gamma\right)e^{-i\varphi} \\ \left(1 - 2\cos^2\frac{\theta}{2}\sin^2\gamma\right)e^{i\varphi} & -\cos^2\frac{\theta}{2}\sin\gamma\cos\gamma \end{bmatrix} \end{aligned} \tag{S20}$$

Since the quantum system is a non-Abelian system, its geometric feature is described by the Wilczek-Zee phase. The topological properties of the manifold is characterized by geometric tensor which is written as

$$\begin{aligned}
Q^{\theta\theta} &= \frac{1}{4}\begin{bmatrix}1 & 0\\ 0 & 1\end{bmatrix}\\
Q^{\gamma\gamma} &= \frac{1}{4}\sin^2\theta\begin{bmatrix}1 & 0\\ 0 & 1\end{bmatrix}\\
Q^{\varphi\varphi} &= \frac{1}{4}\sin^2\theta\sin^2\gamma\begin{bmatrix}1 & 0\\ 0 & 1\end{bmatrix}\\
Q^{\theta\gamma} &= \frac{1}{4}\sin\theta\begin{bmatrix}0 & e^{-i\varphi}\\ -e^{i\varphi} & 0\end{bmatrix}\\
Q^{\theta\varphi} &= \frac{i}{4}\sin\theta\sin\gamma\begin{bmatrix}\sin\gamma & \cos\gamma e^{-i\varphi}\\ \cos\gamma e^{i\varphi} & -\sin\gamma\end{bmatrix}\\
Q^{\gamma\varphi} &= \frac{i}{4}\sin^2\theta\sin\gamma\begin{bmatrix}-\cos\gamma & \sin\gamma e^{-i\varphi}\\ \sin\gamma e^{i\varphi} & \cos\gamma\end{bmatrix}
\end{aligned} \tag{S21}$$

The corresponding quantum metric tensors are

$$\begin{aligned}
&g^{\theta\theta} = \frac{1}{4}\begin{bmatrix}1 & 0\\ 0 & 1\end{bmatrix}, \quad g^{\gamma\gamma} = \frac{1}{4}\sin^2\theta\begin{bmatrix}1 & 0\\ 0 & 1\end{bmatrix}, \quad g^{\varphi\varphi} = \frac{1}{4}\sin^2\theta\sin^2\gamma\begin{bmatrix}1 & 0\\ 0 & 1\end{bmatrix},\\
&g^{\theta\gamma} = \frac{1}{4}\sin\theta\begin{bmatrix}0 & \cos\varphi\\ \cos\varphi & 0\end{bmatrix}, \quad g^{\theta\varphi} = \frac{1}{4}\sin\theta\sin\gamma\begin{bmatrix}0 & \cos\gamma\sin\varphi\\ -\cos\gamma\sin\varphi & 0\end{bmatrix},\\
&g^{\gamma\varphi} = \frac{1}{4}\sin^2\theta\sin\gamma\begin{bmatrix}0 & \sin\gamma\sin\varphi\\ -\sin\gamma\sin\varphi & 0\end{bmatrix},
\end{aligned} \tag{S22}$$

The topological invariant including winding number and geometric phase are closely related to Berry curvatures, which can be derived from Berry connection and geometric tensor. According the relation $F^{\mu\nu}(\lambda) = \frac{\partial A^\nu}{\partial\lambda_\mu} - \frac{\partial A^\mu}{\partial\lambda_\nu} - i\left[A^\mu, A^\nu\right]$ and $F^{\mu\nu} = i(Q^{\mu\nu} - [Q^{\mu\nu}]^\dagger)$ we can obtain

$$\begin{aligned}
F^{\theta\gamma} &= [F^{\gamma\theta}]^\dagger = \frac{1}{2}\sin\theta\begin{bmatrix}0 & e^{-i\varphi}\\ -e^{-i\varphi} & 0\end{bmatrix},\\
F^{\theta\varphi} &= [F^{\varphi\theta}]^\dagger = i\frac{1}{2}\sin\theta\sin\gamma\begin{bmatrix}\sin\gamma & \cos\gamma e^{-i\varphi}\\ \cos\gamma e^{i\varphi} & -\sin\gamma\end{bmatrix},\\
F^{\gamma\varphi} &= [F^{\varphi\gamma}]^\dagger = i\frac{1}{2}\sin^2\theta\sin\gamma\begin{bmatrix}-\cos\gamma & \sin\gamma e^{-i\varphi}\\ \sin\gamma e^{i\varphi} & \cos\gamma\end{bmatrix}.
\end{aligned} \tag{S23}$$

and the null-terms are not listed here.

IV. BHZ MODEL UNDER MORRIS–SHORE TRANSFORMATION

The Hamiltonian of the BHZ model is constructed in the four-dimensional space spanned with parameters $\{\theta, \gamma, \varphi\}$. This Hamiltonian can be simulated in our quantum circuit, but to improve the experimental fidelity we deform it into a two-level subspace by the Morris–Shore transformation U_{MS}, of which matrix is written as

$$U_{MS} = \frac{1}{2}\begin{bmatrix}
\frac{\cos\gamma}{\cos\left(\frac{\gamma}{2}+\frac{\pi}{4}\right)} & \frac{(1-\sin\gamma)e^{-i\varphi}}{\cos\left(\frac{\gamma}{2}+\frac{\pi}{4}\right)} & 0 & 0\\
0 & 0 & \frac{\cos\gamma}{\cos\left(\frac{\gamma}{2}+\frac{\pi}{4}\right)} & \frac{(1-\sin\gamma)e^{i\varphi}}{\cos\left(\frac{\gamma}{2}+\frac{\pi}{4}\right)}\\
\frac{e^{i\varphi}\cos\gamma}{\sin\left(\frac{\gamma}{2}+\frac{\pi}{4}\right)} & -\frac{1+\sin\gamma}{\sin\left(\frac{\gamma}{2}+\frac{\pi}{4}\right)} & 0 & 0\\
0 & 0 & \frac{e^{-i\varphi}\cos\gamma}{\sin\left(\frac{\gamma}{2}+\frac{\pi}{4}\right)} & -\frac{1+\sin\gamma}{\sin\left(\frac{\gamma}{2}+\frac{\pi}{4}\right)}
\end{bmatrix} \tag{S24}$$

After the transformation, the modified Hamiltonian can be rewritten as

$$H_s^{'} = \begin{bmatrix}
\cos\theta & e^{-i\varphi}\sin\theta & 0 & 0\\
e^{i\varphi}\sin\theta & -\cos\theta & 0 & 0\\
0 & 0 & \cos\theta & -e^{i\varphi}\sin\theta\\
0 & 0 & -e^{-i\varphi}\sin\theta & -\cos\theta
\end{bmatrix}, \tag{S25}$$

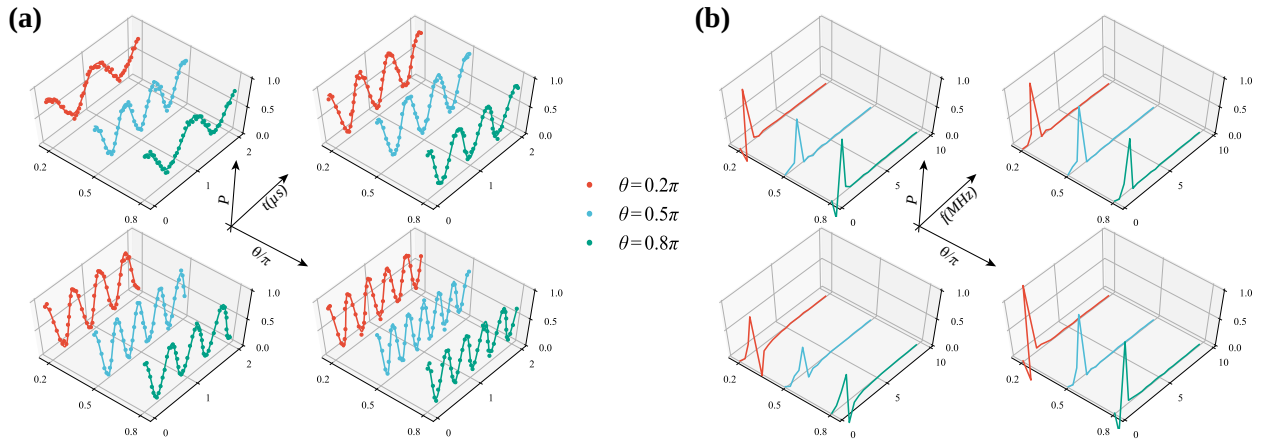

FIG. S4. **Resonant Rabi oscillation under different types of parametric modulation in subspace $\mathcal{S}_{22}$. (a)** The Rabi oscillations are obtained at various θ. We point out that the occupation states are located in the lower-band states with the eigenvalue E_-. From left to right and top to bottom, we show the Rabi oscillations under the single modulation: φ, θ; and two parameters modulation φ and θ at $\delta\phi = 0$, and $\delta\phi = 0.5\pi$, respectively. **(b)** The Rabi oscillation frequencies are extracted from **(a)** by FFT.

which is the parameters space $\{\theta, \varphi\}$. Therefore, the metric tensor Eq. S22 deforms to

$$g^{\theta\theta} = \frac{1}{4}\begin{bmatrix} 1 & 0 \\ 0 & 1 \end{bmatrix}, \quad g^{\varphi\varphi} = \frac{1}{4}\sin^2\theta \begin{bmatrix} 1 & 0 \\ 0 & 1 \end{bmatrix}, \quad g^{\theta\varphi} = \frac{1}{4}\sin\theta \begin{bmatrix} 0 & \sin\varphi \\ -\sin\varphi & 0 \end{bmatrix}, \tag{S26}$$

which is obtained in our experiment. As we explain in the main text, this simplification does not fade our quantum simulations. The new Hamiltonian captures the features of the band structure of the topological material, while the measured spin Chern number reveals the physical properties of the quantum system. Besides, in practice, this protocol can greatly reduce the experimental error, such as the imperfection of the applied pulse in parametric modulation.

Since the MS transformation reduces the parameter dimension, only parts of the quantum geometric metric were measured. Similar to projecting along different axes in quantum of state tomography, we need to 'rotate' the Hamiltonian to read different parts of the metric tensor, then we can construct the entire QGT. For instance, to obtain the metric tensor related to the parameter γ, we can apply the Hamiltonian Eq. S16 with the unitary transformation to exchange the diagonal and anti-diagonal elements of the matrix, such as

$$U_R = \begin{bmatrix} \frac{1}{\sqrt{2}} & 0 & 0 & -\frac{1}{\sqrt{2}} \\ 0 & \frac{1}{\sqrt{2}} & -\frac{1}{\sqrt{2}} & 0 \\ 0 & \frac{1}{\sqrt{2}} & \frac{1}{\sqrt{2}} & 0 \\ \frac{1}{\sqrt{2}} & 0 & 0 & \frac{1}{\sqrt{2}} \end{bmatrix}, \tag{S27}$$

then we measure the $Q^{\gamma\gamma}, Q^{\gamma\varphi}$, and $Q^{\theta\gamma}$ with corresponding MS operations.

V. MEASUREMENT OF NON-ABELIAN QUANTUM GEOMETRIC TENSOR

Periodic drivings.— For simplicity, the Hamiltonian Eq. (S13) of the non-Abelian QGT in experiment is reduced to

$$H_s = \begin{pmatrix} \Delta & \Omega e^{-i\varphi} & 0 & 0 \\ \Omega e^{i\varphi} & -\Delta & 0 & 0 \\ 0 & 0 & \Delta & -\Omega e^{i\varphi} \\ 0 & 0 & -\Omega e^{-i\varphi} & -\Delta \end{pmatrix} \tag{S28}$$

with $\Delta = \delta_{12} = \delta_{34}$, $\Omega = |g_{12}J_1(\frac{\omega_{12}^T}{\Delta_{12}})| = |g_{34}J_1(\frac{\omega_{34}^T}{\Delta_{34}})|$, $\varphi = \varphi_{12} - \frac{\omega_{12}^T}{\Delta_{12}}\sin\varphi_{12} = -\varphi_{34} - \frac{\omega_{34}^T}{\Delta_{34}}\sin\varphi_{34}$, respectively. Therefore, the non-Abelian Hamiltonian Eq. (5) in main text can be obtained by introducing parameters $\theta = \arctan\frac{\Omega}{\Delta}$

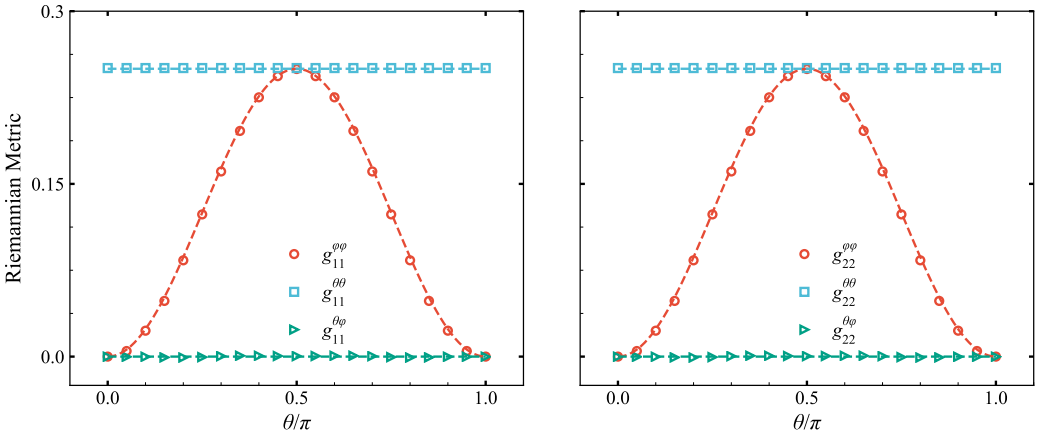

FIG. S5. **Simulation results of the quantum geometric tensor.** Simulation results under the experimental conditions in the main text Fig. 4 (a). The dashed lines are the theoretical expectations while the points denote the simulation results.

and $\Omega_0 = \sqrt{\Delta^2 + \Omega^2}$. As elaborated in the main text, the weak periodic parametric modulation field $A\cos(\omega t + \phi_\mu)$ has been introduced, in which the amplitude A and frequency ω satisfy $A \ll \omega$ to meet the condition for the perturbation to extract the QGT by measuring Rabi oscillations. For facilitating the state initialization and improving the measurement fidelity, we introduce a unitary operator U_R as used in Ref. [21] to rotate the frame $U_R^\dagger H_s U_R$ in the experiment to keep the instantaneous eigenstate of the Hamiltonian in the $|1000\rangle$ or $|0010\rangle$ at $t = 0$. According to Eq. (2) an Eq. (3) in main text, we can construct the weak periodic parametric fields

$$\begin{aligned}
\delta\omega_1^{\theta\theta}(t) &= A\cos(\omega t + \phi_\theta)\cos(\Delta t - \omega t + \varphi),\\
\delta\omega_2^{\theta\theta}(t) &= A\cos(\omega t + \phi_\theta)\cos(\omega t - \Delta t - \varphi),\\
\delta\omega_1^{\varphi\varphi}(t) &= A\sin\theta\cos(\omega t + \phi_\varphi)\cos(\Delta t - \omega t + \varphi),\\
\delta\omega_2^{\varphi\varphi}(t) &= A\sin\theta\cos(\omega t + \phi_\varphi)\cos(\omega t - \Delta t - \varphi),\\
\delta\omega_1^{\theta\varphi}(t) &= A\sin\theta\cos(\omega t + \phi_\varphi)\cos(\Delta t - \omega t + \varphi) + A\cos(\omega t + \phi_\theta)\cos(\Delta t - \omega t + \varphi),\\
\delta\omega_2^{\theta\varphi}(t) &= A\sin\theta\cos(\omega t + \phi_\varphi)\cos(\Delta t - \omega t - \varphi) + A\cos(\omega t + \phi_\theta)\cos(\Delta t - \omega t - \varphi),
\end{aligned} \tag{S29}$$

which correspond the different QGT measurements $Q_{11}^{\theta\theta}$, $Q_{22}^{\theta\theta}$, $Q_{11}^{\varphi\varphi}$, $Q_{22}^{\varphi\varphi}$, $Q_{11}^{\theta\varphi}$, and $Q_{22}^{\theta\varphi}$, respectively.

Supplementary results.— Since the Rabi signals oscillate between the eigenstates, which can be independently measured by multi-tone readout, the QGT can also be extracted by measuring the excited states $|\Psi_1(\lambda)\rangle$. Moreover, for our two-band two-degeneracy system, we can also assume that an occupation of states is located on upper band E_+, making that the QGT under two parameters modulation can be written as

$$Q_{QGT} = Q_{jj}^{\mu\mu} + Q_{jj}^{\nu\nu} - e^{-i\delta\phi}Q_{jj}^{\mu\nu} - e^{i\delta\phi}Q_{jj}^{\nu\mu}, \tag{S30}$$

which is different with the one in main text. Therefore, the QGT terms in Eq. (6) in main text become

$$[Q^{\theta\theta}]^+ = \frac{1}{4}\begin{bmatrix}1 & 0\\ 0 & 1\end{bmatrix}, \qquad [Q^{\varphi\varphi}]^+ = \frac{1}{4}\sin^2\theta\begin{bmatrix}1 & 0\\ 0 & 1\end{bmatrix}, \qquad [Q^{\theta\varphi}]^+ = \frac{i}{4}\sin\theta\begin{bmatrix}1 & 0\\ 0 & -1\end{bmatrix}, \tag{S31}$$

and here, we supply the results about the Rabi oscillations in subspace $\mathcal{S}_{22}$, as shown in Fig. S4(a) and (b), which are measured under the ground state $|\Psi_0(\lambda)\rangle$, respectively.

Simulation results.— Here, we have supplied some simulation results to clarify the differences between our experimental results and theoretical expectations in the main text Fig. 4(a). We note that for numerical simulation, the modulation amplitude $A^{'}/2\pi = 3.05$ MHz we used is slightly larger than the ideal value 3 MHz to cancel the shifting amplitude due to the imperfect modulation pulses in practical used. This shifting amplitude can be calibrated according to the measurement of Rabi oscillations used in the experiment procedure. As shown in Fig. S5, the simulation results (the dashed lines) are in good agreement with the theoretical expectations (the points). Compared with these simulation results, we believe that these differences mainly come from the uncertainty of our calibrated parameters (such as the frequencies of qubits, the modulation amplitude A, etc.) rather than the decoherence times. In experiment, we usually obtain the bigger values than theoretical expectations, because the Rabi frequency we measured

$\Omega_0 = \sqrt{\Omega^2 + \Delta^2}$ includes the detuning ($\Delta \neq 0$) while we set the ideal detuning ($\Delta = 0$) in Fig. 4(a). Here, the detuning is usually caused by the uncertainty of qubits frequencies.

In our experiment, the QGT can be obtained according to the Rabi frequency $\Omega_0 = \sqrt{A^2 Q_{QGT} + \Delta}$ (Eq. (2) in main text) if the modulation amplitude A and frequency ω satisfy $A \ll \omega$, where Q_{QGT} is directly related to the QGT terms we measured (Details see the sentences below Eq. (2) in main text). First, the decoherence times T_1 and T_2 lead to the decay of Rabi oscillations with the Rabi frequency $\Omega_0 \sim A\sqrt{Q_{QGT}}$. If the amplitude A is not large enough, the oscillations is too slow hence the decay limits the QGT measurement in the system with short decoherence times. In addition, the stability of a system is also very important, because the uncertainty of the calibrated parameters (such as the detuning Δ) will introduce the inaccuracy of the Rabi frequency. Nevertheless, in most cases, the measurement of the Rabi frequency is a very simple but reliable method, hence the results obtained agree with the theory well.

[1] J. Koch *et al.*, Phys. Rev. A **76** 042319, (2007).
[2] R. Barends *et al.*, Phys. Rev. Lett. **111** 080502, (2013).
[3] A. Kanda, M. Wada, Y. Hamamoto, and Y. Ootuka, Phys. E (Amsterdam, Neth.) **29** 707, (2005).
[4] Z. Chen *et al.*, Appl. Phys. Lett. **104** 052602, (2014).
[5] A. Blais, R.-S. Huang, A. Wallraff, S. M. Girvin, and R. J. Schoelkopf, Phys. Rev. A **69** 062320, (2004).
[6] N. Didier, E. A. Sete, M. P. da Silva, and C. Rigetti, Phys. Rev. A **97** 022330, (2018).
[7] D. Li *et al.*, Appl. Phys. Lett. **118** 104003, (2021).
[8] M.-H. Yung, arXiv:0707.2779 [quant-ph] (2007).
[9] H. Weisbrich, G. Rastelli, and W. Belzig, Phys. Rev. Research **3** 033122, (2021).
[10] J. R. Morris and B. W. Shore, Phys. Rev. A **27** 906, (1983).
[11] B. W. Shore, J. Mod. Opt. **61** 787, (2014).
[12] K. N. Zlatanov, G. S. Vasilev, and N. V. Vitanov, Phys. Rev. A **102** 063113, (2020).
[13] B. A. Bernevig, T. L. Hughes, and S.-C. Zhang, Science **314** 1757, (2006).
[14] M. Z. Hasan and C. L. Kane, Rev. Mod. Phys. **82** 3045, (2010).
[15] Q.-X. Lv *et al.*, Phys. Rev. Lett. **127** 136802, (2021).
[16] C. L. Kane and E. J. Mele, Phys. Rev. Lett. **95** 146802, (2005).
[17] C. L. Kane and E. J. Mele, Phys. Rev. Lett. **95** 226801, (2005).
[18] L. Sheng, D. N. Sheng, C. S. Ting, and F. D. M. Haldane, Phys. Rev. Lett. **95** 136602, (2005).
[19] D. N. Sheng, Z. Y. Weng, L. Sheng, and F. D. M. Haldane, Phys. Rev. Lett. **97** 036808, (2006).
[20] L. Sheng, H.-C. Li, Y.-Y. Yang, D.-N. Sheng, and D.-Y. Xing, Chin. Phys. B **22** 067201, (2013).
[21] X. Tan *et al.*, Phys. Rev. Lett. **122** 210401, (2019).